

# A Space Mapping Methodology for Defect Characterization from Magnetic Flux Leakage Measurements

Reza K. Amineh, Slawomir Koziel, Natalia K. Nikolova, John W. Bandler, and James P. Reilly

**Abstract**—We present an inversion methodology for defect characterization using the data from magnetic flux leakage (MFL) measurements. We use a single tangential component of the leakage field as the MFL response. The inversion procedure employs the space mapping (SM) methodology. Space mapping is an efficient technique that shifts the optimization burden from a computationally expensive accurate (fine) model to a less accurate (coarse) but fast model. Here the fine model is a finite-element method (FEM) simulation, while the coarse model is based on analytical formulas. We achieve good estimation of the defect parameters using just a few FEM simulations, which leads to substantial savings in computational cost as compared to other optimization approaches. We examine the efficiency of the proposed inversion technique in estimating the shape parameters of rectangular and cylindrical defects in steel pipes. Our results show good agreement between the actual and estimated defect parameters.

**Index Terms**— Crack sizing, magnetic flux leakage (MFL), magnetic inverse problems, space mapping optimization.

## I. INTRODUCTION

THE MAGNETIC Flux Leakage (MFL) technique plays an important role in the nondestructive evaluation (NDE) of buried oil and gas pipelines in order to find metal-loss regions usually caused by corrosion, fatigue, etc. The size and shape of the defects can be obtained by studying the distribution of the MFL output signal. After the leakage field is measured, an inverse problem must be solved so that the shape characteristics of the flaw, such as width, length and depth can be estimated. The correct assessment of this information is vital in order to determine critical regions in the pipelines.

The MFL inversion techniques often use an iterative approach where a forward model calculates the leakage field for a given set of defect parameters (illustrated in Fig. 1).

This work was supported by a collaborative research development (CRD) grant of the Natural Sciences and Engineering Council of Canada (NSERC) and Intratech Inline Inspection Services Ltd., grant number CRDPJ 349624-06, NSERC under Grants RGPIN7239-06 and STPGP336760-06, and by Bandler Corporation.

R. K. Amineh (e-mail: [khalajr@mcmaster.ca](mailto:khalajr@mcmaster.ca)), N. K. Nikolova (phone: 905-525-3189; fax: 905-521-2922; e-mail: [talina@mcmaster.ca](mailto:talina@mcmaster.ca)), J. W. Bandler (e-mail: [j.bandler@ieee.org](mailto:j.bandler@ieee.org)), and J. P. Reilly (e-mail: [reillyj@mcmaster.ca](mailto:reillyj@mcmaster.ca)) are with the Department of Electrical and Computer Engineering, McMaster University, Hamilton, Ontario L8S 4K1, Canada.

S. Koziel (e-mail: [koziel@ru.is](mailto:koziel@ru.is)) is with the School of Science and Engineering, Reykjavik University, IS-103 Iceland.

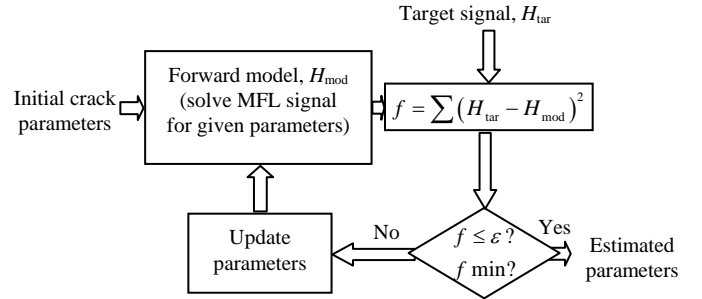


Fig. 1. Flowchart of a conventional iterative procedure for MFL inversion.  $H_{\text{mod}}$  is the field calculated by the forward model.  $H_{\text{tar}}$  is field measured by Hall effect sensors after subtracting the applied field.  $\epsilon$  is the termination criterion.

Three major groups of forward models are commonly used. The first group involves numerical simulations typically based on the finite element method (FEM) [1]–[3]. These models provide accurate results but the drawback is that they are computationally very demanding. The second group consists of closed-form analytical formulas for defects of certain canonical shapes [4]–[7]. These models typically utilize magnetic poles or a dipolar charge on the defect walls. They are very fast but less accurate and versatile due to the assumptions made in deriving the analytical formulas [5][7]. The third group of forward MFL models is based on artificial neural networks for two-dimensional and three-dimensional flaws [8]–[12]. These models are fast but are limited to the region in parameter space for which the neural network is trained.

The availability of the forward models based on FEM simulations [1]–[3] and the analytical formulas [4]–[7] prompts us to employ space mapping (SM) optimization in the defect parameter estimation from MFL data. SM exploits in an iterative manner the two models: an expensive or “fine” model which is very accurate but expensive or time-consuming, and the so called “coarse” model, which is less accurate but cheaper or faster to evaluate [13]–[17]. Provided that the misalignment between the fine and coarse model is not severe, SM-based algorithms typically provide excellent results after only a few evaluations of the fine model. They are far more efficient than the direct optimization of the fine model alone. The fine model data is utilized in the SM algorithm to update

the coarse model iteratively during the optimization process and to create the so-called surrogate model. Thus, SM optimization allows us to benefit from the accuracy of the FEM simulations as a fine model and the speed of the analytical formulas as a coarse model. Based on this scheme, one can significantly reduce the CPU time necessary to characterize the defect parameters.

Here, defect characterization using SM-based optimization is performed for two common types of defects in pipelines—rectangular and cylindrical defects. The results of parameter estimation for some sample defects demonstrate the efficiency of the SM-based optimization as a reliable and fast inversion method, especially in comparison with classical methods performing direct optimization of the FEM model.

## II. MAGNETIC FLUX LEAKAGE MEASUREMENT

MFL tools use permanent magnets to magnetize the pipe's wall to near saturation flux density. If the wall's thickness is reduced by the presence of a defect, a higher fraction of the magnetic flux leaks from the wall into the air inside and outside the pipe. This leakage flux is detected by a Hall sensor and is used to estimate the shape and size of the defect. Fig. 2(a) shows the MFL setup for the detection and evaluation of a rectangular crack with length  $l$ , width  $w$ , and depth  $d$ . Fig. 2(b) shows a similar illustration of a cylindrical defect with radius  $R$  and depth  $D$ . In this work, we monitor the  $y$ -component of the magnetic field as the MFL response.

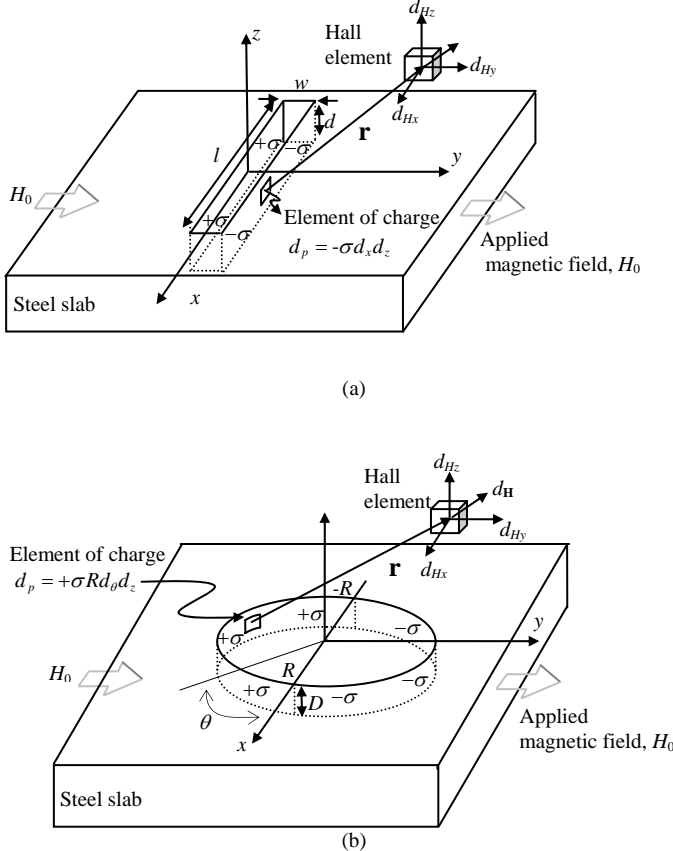


Fig. 2. Dipolar representation of defect; (a) rectangular, (b) cylindrical.

### A. Analytical Models to Predict MFL Response

In all analytical expressions for the MFL signal [4]-[7], it is assumed that the crack is filled with homogeneously distributed magnetic dipoles, i.e., that the surface density of the magnetic charge has a constant value along the crack walls.

Edwards and Palmer [4] presented analytical solutions for the leakage field of a surface-breaking crack as a function of the applied magnetic field strength, the permeability and the crack dimensions. Also, they approximated the MFL response for a semi-elliptical surface-breaking cavity by an equivalent rectangular slot with constant polarity  $\sigma_s$ , positive poles on one face ( $\sigma_s = +\sigma$ ) and negative poles on the other ( $\sigma_s = -\sigma$ ). Then, the differential charge element  $d_p$  in a position  $(x, y, z)$  possesses a charge proportional to its area [4]

$$d_p = \sigma_s dx dz. \quad (1)$$

The magnetic field  $\mathbf{H}$  is calculated at all observation points by integrating the magnetic field due to all charge elements  $d_p$ :

$$\mathbf{H} = \iint_{(x,z) \in S} \frac{d_p}{4\pi r^3} \cdot \mathbf{r} \quad (2)$$

where  $S$  is the cylindrical surface of the crack wall and  $\mathbf{r}$  is the distance vector from the point of integration to the point of observation.

Similar to the previous analytical expressions for surface-breaking cracks, a dipolar magnetic charge model has been developed for cylindrical pit defects [5]. As shown in Fig. 2(b), half of the cylinder wall develops positive magnetic charge density  $+\sigma$  while the other half has negative charge density  $-\sigma$ . The angle  $\theta$  is measured from the positive  $x$ -axis to an element of magnetic charge,  $d_p$ . The differential element  $d_p$  has coordinates  $(R \cos \theta, R \sin \theta, z)$  and a charge proportional to its area [5]

$$d_p = \sigma R d\theta dz. \quad (3)$$

The magnetic field  $\mathbf{H}$  is calculated using the same integral as in (2) but over a circular wall  $S$ .

It has been shown that the simplifying assumptions made in deriving the analytical expressions, especially neglecting the local variations in the magnetization and the permeability around the crack mouth, lead to errors in calculating the leakage field. This indicates that the distribution of the magnetic dipoles  $\sigma$  along the crack depth are in fact not constant [5][7].

### B. FEM Simulations to Predict MFL Response

In MFL-type NDE, we deal with a highly nonlinear system involving a permanent magnet and steel. The Maxwell's equations in a nonlinear permanent magnet system lead to [21]

$$\nabla \times \nabla \times \mathbf{A} = \mu_0 (\mathbf{J} + \nabla \times \mathbf{M}) \quad (4)$$

where  $\mu_0$ ,  $\mathbf{J}$  and  $\mathbf{A}$  are the permeability of vacuum, the current density and the magnetic vector potential, respectively. The magnetization  $\mathbf{M}$  is a non-linear function of  $\mathbf{B} = \nabla \times \mathbf{A}$ .

Therefore, the nonlinear equation (4) is solved iteratively<sup>1</sup>.

A nonlinear structural FEM using Maxwell v. 11 [22] is used for simulating the three-dimensional (3-D) magnetic field around and inside a surface crack in a steel slab. Fig. 3 shows the model geometry. Steel\_1010 is selected from the simulator's library as the material type for the steel slab.

In order to decrease the computational time and still maintain good accuracy, a simplified model of the magnetizer is used. The steel slab is magnetized with two parallel magnets (Fig. 3). NDFe35 is selected as the magnet material. It magnetizes the steel plate in the  $y$ -direction (Fig. 3) with a coercivity such that the operating point is in the knee area of the B-H curve for Steel\_1010. This is desirable because it leads to the maximum signal-to-noise ratio for obtaining the leakage crack signal [21].

Some additional boundary conditions are set to enforce the magnetic field inside the metal to be parallel to the  $y$ -axis. These boundary conditions are: (a) zero normal component of the magnetic field to all faces of the magnetizers except the faces which are parallel to the  $x$ - $z$  plane; (b) zero tangential components of the magnetic field at the faces of the magnetizers which are parallel to the  $x$ - $z$  plane; (c) zero normal component of the magnetic field at the faces of the steel which are parallel to the  $y$ - $z$  plane.

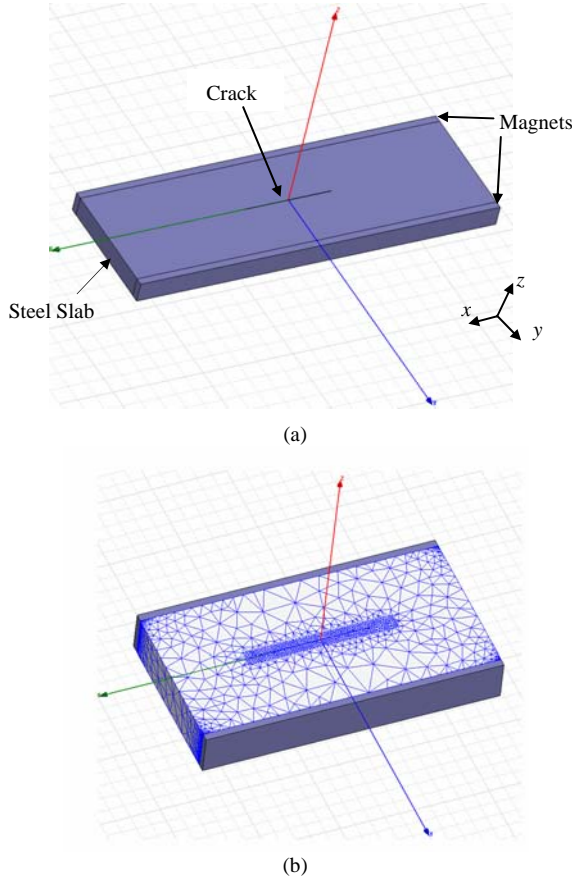


Fig. 3. 3-D view of the simulated model in Maxwell v. 11: (a) structure, (b) FEM mesh on the surface of the metal slab with enforced refinement of elements in the region around the crack.

<sup>1</sup> Throughout, we denote 3-D field vectors in bold, while matrices and column vectors are in bold italics.

It is worth noting that the results of the simulated MFL signals using similar methodology and their corresponding measured signals for rectangular cracks have been presented in [23]. They show good agreement.

### III. SPACE MAPPING OPTIMIZATION

Space mapping (SM) is a recognized engineering optimization methodology that encompasses a number of efficient approaches [13]-[18]. The main idea behind SM is that the direct optimization of an accurate but computationally expensive high fidelity or “fine” model of interest is replaced by the iterative optimization and updating of a so-called “coarse” model (less accurate but much cheaper to evaluate). An example of a fine model would be a device analyzed using an electromagnetic simulator; the coarse model might be a circuit equivalent of the device evaluated using a conventional circuit simulator. Provided that the misalignment between the fine and coarse models is not significant, SM-based algorithms typically provide excellent results after only a few evaluations of the fine model. In contrast, direct optimization typically requires dozens or hundreds of evaluations and often fails to provide acceptable results.

Let  $\mathbf{R}_f: X_f \rightarrow R^m$  denote the response vector of the fine model of a given device, where  $X_f \subseteq R^n$ . Our goal is to solve

$$\mathbf{x}_f^* = \arg \min_{\mathbf{x} \in X_f} U(\mathbf{R}_f(\mathbf{x})) \quad (5)$$

where  $U: R^m \rightarrow R$  is a given objective function. In many engineering problems, we are concerned with the so-called minimax objective function: if we denote the fine model response components by  $\mathbf{R}_f = [R_{f,1} \dots R_{f,m}]^T$ , the lower specification vector by  $\mathbf{R}_l = [R_{l,1} \dots R_{l,m}]^T$ , and the upper specification vector by  $\mathbf{R}_u = [R_{u,1} \dots R_{u,m}]^T$ , then we require that  $R_{f,i} \leq R_{u,i}$  for  $i \in I_u$  and  $R_{f,i} \geq R_{l,i}$  for  $i \in I_l$ , where  $I_l, I_u \subset \{1, 2, \dots, m\}$ . The minimax objective function is given by

$$U(\mathbf{R}_f) = \min \left\{ \max_{i \in I_u} (R_{f,i} - R_{u,i}), \max_{i \in I_l} (R_{l,i} - R_{f,i}) \right\}. \quad (6)$$

In some problems,  $U$  can be defined by a norm, i.e.,

$$U(\mathbf{R}_f) = \|\mathbf{R}_f - \mathbf{R}_{spec}\| \quad (7)$$

where  $\mathbf{R}_{spec} = [R_{spec,1} \dots R_{spec,m}]^T$  is the target response.

We consider the fine model to be expensive to compute and solving (5) by direct optimization to be impractical. Instead, we use surrogate models, i.e., models that are supposed to be good local representations of the fine model and computationally cheap, hence suitable for iterative optimization. According to the SM approach, the surrogate is built based on the coarse model as well as some auxiliary mappings. The mapping parameters are adjusted during the so-called parameter extraction process in order to reduce misalignment between the fine model and the surrogate. The process of updating the surrogate model is performed iteratively using the fine model data accumulated during the optimization process. We consider an optimization algorithm

that generates a sequence of points  $\mathbf{x}^{(i)}$ ,  $i = 0, 1, 2, \dots$ , and a family of surrogate models  $\mathbf{R}_s^{(i)}$ , so that

$$\mathbf{x}^{(i+1)} = \arg \min_{\mathbf{x}} U(\mathbf{R}_s^{(i)}(\mathbf{x})). \quad (8)$$

Let  $\mathbf{R}_c : X_f \rightarrow R^m$  denote the response vector of the coarse model that describes the same object as the fine model but is less accurate and much faster to evaluate. Let  $\bar{\mathbf{R}}_s$  be a generic SM surrogate model, i.e., the coarse model composed with suitable SM transformations. At iteration  $i$  the surrogate model  $\mathbf{R}_s^{(i)}$  is defined as

$$\mathbf{R}_s^{(i)}(\mathbf{x}) = \bar{\mathbf{R}}_s(\mathbf{x}, \mathbf{p}^{(i)}) \quad (9)$$

where

$$\mathbf{p}^{(i)} = \arg \min_{\mathbf{p}} \sum_{k=0}^i w_{i,k} \|\mathbf{R}_f(\mathbf{x}^{(k)}) - \bar{\mathbf{R}}_s(\mathbf{x}^{(k)}, \mathbf{p})\| \quad (10)$$

is a vector of model parameters and  $w_{i,k}$  are weighting factors. Typically, we put  $w_{i,k} = 1$  for all  $i$  and  $k$ .

A variety of SM surrogate models is available [17], [18]. One of the most popular approaches is the so-called input SM [13], in which the generic SM surrogate model takes the form  $\bar{\mathbf{R}}_s(\mathbf{x}, \mathbf{p}) = \bar{\mathbf{R}}_s(\mathbf{x}, \mathbf{B}, \mathbf{c}) = \mathbf{R}_c(\mathbf{B} \cdot \mathbf{x} + \mathbf{c})$ . Another popular approach is the so-called output SM where the surrogate model is defined as  $\bar{\mathbf{R}}_s(\mathbf{x}, \mathbf{p}) = \bar{\mathbf{R}}_s(\mathbf{x}, \mathbf{d}) = \mathbf{R}_c(\mathbf{x}) + \mathbf{d}$ , where  $\mathbf{d}$  is a correction term accounting for the difference between the fine and coarse model responses at iteration  $i$ , so that  $\mathbf{d}^{(i)} = \mathbf{R}_f(\mathbf{x}^{(i)}) - \mathbf{R}_c(\mathbf{x}^{(i)})$ . In other words, this output SM ensures zero-order consistency between the fine model and the surrogate [24]. In practice, basic mappings are often combined together in order to create more involved surrogate models. Fig. 4 illustrates the combination of the input and output space mapping approaches.

The choice of SM surrogate type is normally problem dependent. Some methods of assessing the surrogate model as well as the techniques for automatic selection of the surrogate model for a given optimization problem can be found in [25], and [26]. In many cases, including this paper, a suitable model can be found using the following approach: (i) start with the simplest model (e.g., shift-based input space mapping with only parameter  $\mathbf{c}$ ), (ii) perform parameter extraction, (iii) check the matching between the surrogate and the fine model, (iv) if the matching is not sufficient (which can be examined visually by observing model responses), add degrees of freedom and go back to (ii). The model verification may be performed at the starting point so that no extra fine model evaluations are necessary. Also, over-flexibility of the surrogate model should be avoided because it normally degrades its generalization capabilities [26].

Typically, the starting point  $\mathbf{x}^{(0)}$  of the SM optimization algorithm is a coarse model optimal solution, i.e.,  $\mathbf{x}^{(0)} = \arg \min \{\mathbf{x} : U(\mathbf{R}_c(\mathbf{x}))\}$ .

The SM optimization algorithm flow can be described as follows:

*Step 1* Choose the proper coarse model as well as space mapping surrogate type. Set  $i = 0$ .

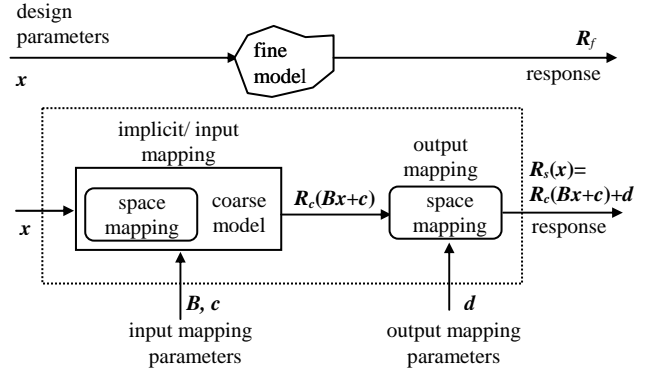


Fig. 4. Fine model and the space mapping surrogate based on input and output SM.

*Step 2* Evaluate the fine model to find  $\mathbf{R}_f(\mathbf{x}^{(i)})$ .

*Step 3* Obtain the surrogate model  $\mathbf{R}_s^{(i)}$  using (9) and (10).

*Step 4* Given  $\mathbf{x}^{(i)}$  and  $\mathbf{R}_s^{(i)}$ , obtain  $\mathbf{x}^{(i+1)}$  using (8).

*Step 5* If the termination condition is not satisfied go to Step 2; else, terminate the algorithm.

Step 3 is the parameter extraction and it plays a crucial role in establishing the surrogate model. Usually, the algorithm is terminated when convergence is obtained or when the user-defined maximum number of iterations is exceeded.

#### IV. INVERSION PROCEDURE BASED ON SM OPTIMIZATION

In this work, we estimate the shape parameters of rectangular and cylindrical defects using SM-based optimization. In case of crack-like rectangular defects, we assume that the width of the crack is very small compared to its length and depth such that the variation of the MFL signal with the width is negligible. Therefore, the inversion problem is a two-variable optimization problem for the length  $l$  and the depth  $d$ , i.e.,  $\mathbf{x} = [l \ d]^T$ . In the case of cylindrical defects, the parameters of interest are the radius  $R$  and the depth  $D$ . The inversion problem is again a two-variable optimization problem, i.e.,  $\mathbf{x} = [R \ D]^T$ . Fig. 5 illustrates the flowchart of the SM-based optimization for estimating the parameters of interest. FEM simulations serve as the fine models and the analytical formulas given by (1)-(3) implemented in Matlab [27] serve as the coarse model. We use the SMF system [28][29] to perform the SM optimization.

The termination condition for the SM algorithm has the following form:

$$\frac{\|\mathbf{x}^{(i+1)} - \mathbf{x}^{(i)}\|}{\|\mathbf{x}^{(i)}\|} < \delta \quad (11)$$

where  $\|\cdot\|$  is the  $l_2$ -norm, and where  $\mathbf{x}^{(i)}$ ,  $i = 0, 1, \dots$ , is the sequence of solutions produced by the SM algorithm, and  $\delta$  is a small user defined constant.

#### V. RESULTS

Results of various simulation tests are presented here to assess the accuracy and the computational efficiency of the proposed inversion technique based on SM optimization. For

this purpose, two rectangular cracks and two cylindrical pits are examined. Tables I and II show the parameter values of these defects. The target MFL responses for all cases are the y-component distributions of the magnetic field monitored at a distance of 3.5 mm above the surface of the metal. These are produced using FEM simulations. We assume that the search

regions for the parameter values are restricted within the following ranges: (a) for rectangular cracks,  $5 \text{ mm} \leq l \leq 65 \text{ mm}$  and  $0.1 \text{ mm} \leq d \leq 4.5 \text{ mm}$ ; and (b) for cylindrical pits,  $0.5 \text{ mm} \leq R \leq 10 \text{ mm}$  and  $0.5 \text{ mm} \leq D \leq 4.5 \text{ mm}$ .

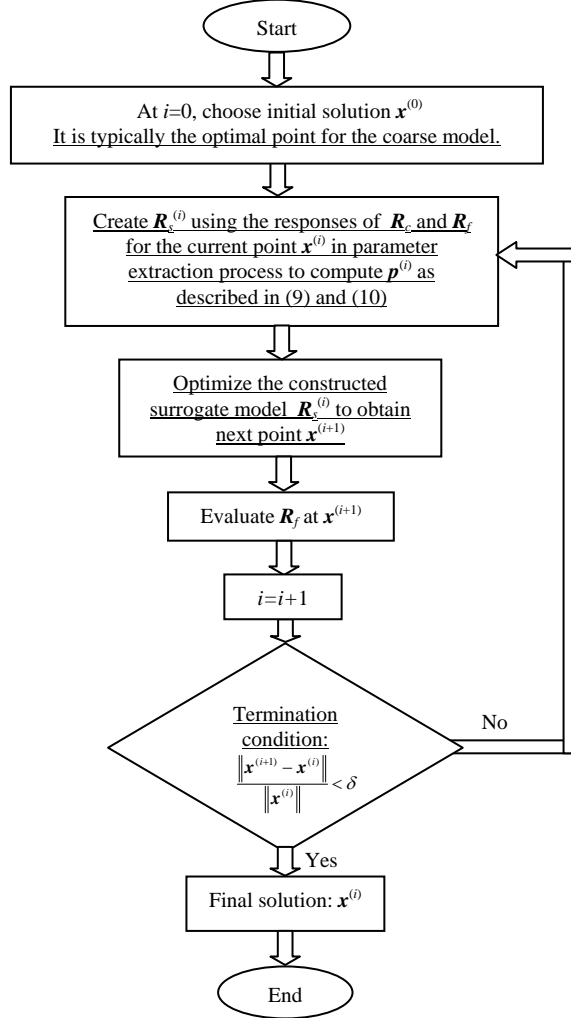


Fig. 5. Flowchart of space mapping optimization.

TABLE I  
LENGTH AND DEPTH FOR THE RECTANGULAR CRACKS

Crack name	Length, $l$ (mm)	Depth, $d$ (mm)
Crack1	15	2.5
Crack2	35	1.5

TABLE II  
RADIUS AND DEPTH FOR THE CYLINDRICAL PITS

Pit name	Radius, $R$ (mm)	Depth, $D$ (mm)
Pit1	3	4
Pit2	5	2

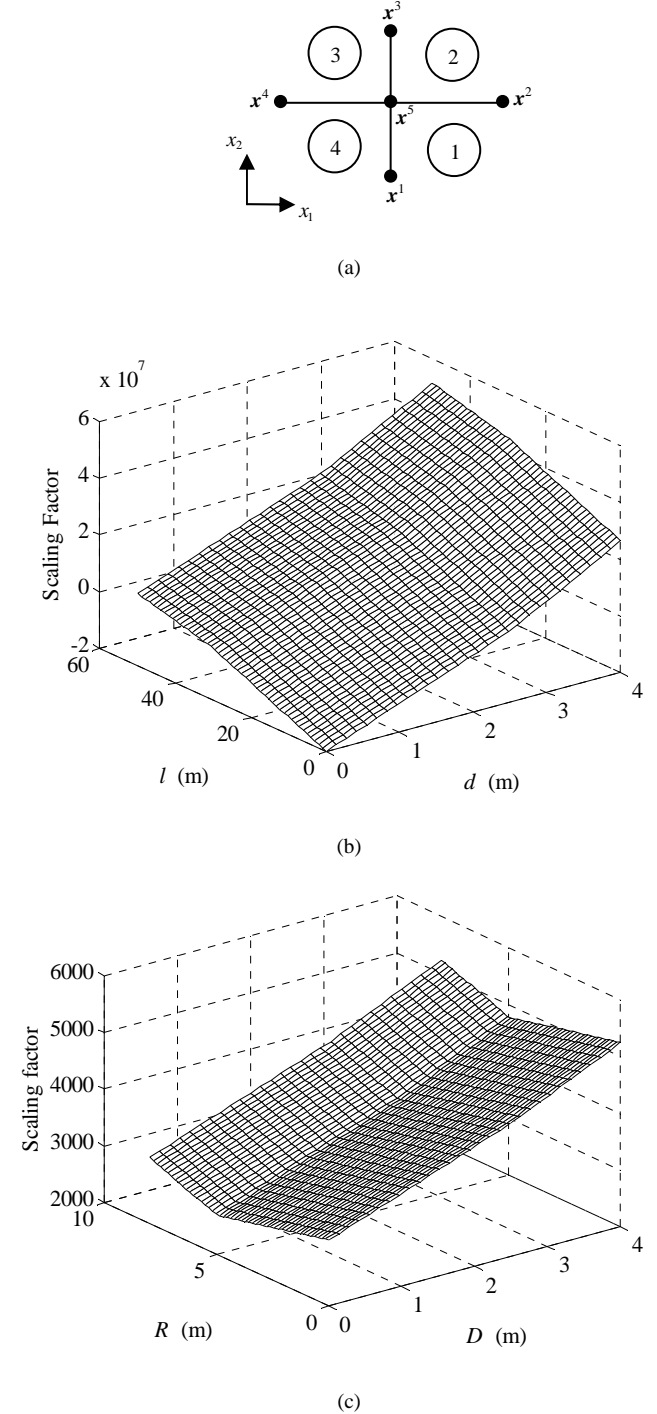


Fig. 6. (a) Constructing the scaling surface from four quadrant surfaces and 5 points (defects), (b) Illustration of scaling surface for rectangular cracks, (c) illustration of scaling surface for rectangular cracks.

TABLE III  
CRACKS (POINTS) USED TO DEFINE 4 SUB-SURFACES IN FIG. 6.

Region No	Defect vertex No.	Parameter Region
1	1, 2, 5	$x_1 \geq x_1^1, x_2 \leq x_2^2$
2	2, 3, 5	$x_1 \geq x_1^1, x_2 \geq x_2^2$
3	3, 4, 5	$x_1 \leq x_1^1, x_2 \geq x_2^2$
4	1, 4, 5	$x_1 \leq x_1^1, x_2 \leq x_2^2$

It should be noted that the performance of a space mapping algorithm depends on the similarity between the fine model and the coarse model, which can be expressed in rigorous mathematical terms (e.g., [18]). Unfortunately, it is difficult to verify whether this similarity is sufficient or not for a given problem because of the lack of fine model data. Therefore, it is beneficial to ensure as good alignment between the coarse and fine model as possible beforehand. In our case, as the maximum amplitudes of the MFL distributions obtained from the coarse and the fine models are substantially different, we use a scaling surface to align them.

The surface describes the coefficient which multiplies the coarse model response to match the corresponding fine model response within the search region. We construct this surface using the coarse and fine model responses for a set of 5 sample defects and defining four quadrant sub-surfaces. These points are selected so that they roughly cover the whole 2-D parameter space of interest. Fig. 6 shows the construction of the scaling surface from 4 quadrant sub-surfaces (1, 2, 3, and 4) defined by 5 defects (points),  $\mathbf{x}^1, \mathbf{x}^2, \mathbf{x}^3, \mathbf{x}^4$ , and  $\mathbf{x}^5$ . Each sub-surface is defined by 3 points and linear interpolation/extrapolation formula. Table III shows the cracks that are used to define the 4 sub-surfaces in Fig. 6. We use the following 2-D inter/extrapolation formula to evaluate the sub-surface  $M$  at any  $\mathbf{x}$ :

$$M(x_1, x_2) = A \cdot x_1 + B \cdot x_2 + C \quad (12)$$

where  $A, B$ , and  $C$  are constants which are computed using the corresponding 3 points to define this sub-surface. For rectangular cracks, the following points (cracks) are used to construct the scaling surface:  $\mathbf{x}^1 = [30 \ 1]^T$ ,  $\mathbf{x}^2 = [50 \ 2.5]^T$ ,  $\mathbf{x}^3 = [30 \ 4]^T$ ,  $\mathbf{x}^4 = [10 \ 2.5]^T$ , and  $\mathbf{x}^5 = [30 \ 2.5]^T$ . The sample points in the case of cylindrical pits are:  $\mathbf{x}^1 = [5 \ 1]^T$ ,  $\mathbf{x}^2 = [8 \ 2.5]^T$ ,  $\mathbf{x}^3 = [5 \ 4]^T$ ,  $\mathbf{x}^4 = [2 \ 2.5]^T$ , and  $\mathbf{x}^5 = [5 \ 2.5]^T$ . Figures 6 (b) and (c) illustrate the constructed scaling surfaces based on the mentioned points for two type of defects. Once we have the scaling surface  $M(\mathbf{x})$ , we use the scaling factor at each  $\mathbf{x}$  to adjust the level of the coarse model response to that of the fine model. It should be noted that the described scaling method has been chosen as a trade-off between the accuracy of the scaling and the computational cost of extra fine model evaluations required to implement the scaling. More accurate scaling (e.g., with a quadratic regression model) would require more fine model data, whereas 5 points together with a piece-wise linear approximation is sufficient for our purposes. The location of the points is not critical, although a factorial-type distribution of points (cf. [30]) is often used.

We would like to mention that the local alignment between

the fine model and the surrogate can also be ensured using an output space mapping as explained in Section III. Unfortunately, when the scaling surfaces are left out and the output space mapping is used instead, the algorithm is not able to find satisfactory solutions in our case. The reason is that the output space mapping surrogate “transfers” the residual (i.e., the difference between the fine and coarse model at the current iteration point) to the new surrogate model optimum, which may be misleading if the overall alignment between the fine and coarse models is too poor, as it is the case when the scaling surfaces are not used.

Prior to starting the SM optimization, the optimal solution of the corresponding coarse model is computed. In particular, the coarse models are directly optimized using the sequential quadratic programming (SQP) method in Matlab optimization toolbox [24]. We examined optimal points,  $\mathbf{x}_c^*$ , obtained from direct optimizations of the coarse models when starting from different initial points. The results demonstrated that the optimization algorithms converge to unique solutions for all investigated defects which are  $[17.38 \ 3.53]^T$ ,  $[34.2 \ 2.46]^T$ ,  $[4.28 \ 2.50]^T$ , and  $[6.07 \ 1.70]^T$  for Crack1, Crack2, Pit1, and Pit2, respectively. A quantitative comparison of the inversion results from the direct optimization of the coarse model is given in Table IV, where the mean relative error (MRE) is defined as:

$$\text{MRE}(\hat{\mathbf{x}}) = \frac{1}{2} \left( \frac{|\mathbf{x}_2 - \hat{\mathbf{x}}_2|}{x_2} + \frac{|\mathbf{x}_1 - \hat{\mathbf{x}}_1|}{x_1} \right) \times 100. \quad (13)$$

where  $\mathbf{x}$  and  $\hat{\mathbf{x}}$  denote the actual and solution points, respectively.

The SM optimization is performed using the input space mapping surrogate model of the form  $\bar{\mathbf{R}}_s(\mathbf{x}, \mathbf{p}) = \mathbf{R}_s(\mathbf{x}, \mathbf{c}) = \mathbf{R}_c(\mathbf{x} + \mathbf{c})$  with the vector  $\mathbf{c}$  obtained through the parameter extraction process (10). This particular model has been chosen because it provides sufficient matching with the fine model, so that there is no need to exploit more involved models in our case. We use the termination condition (11) with  $\delta$  equal to 0.01.

Table IV summarizes the optimization results. The SM initial points, which are the optimal points of the coarse models, are denoted as  $\mathbf{x}_c^*$ . The table also shows the MRE for the coarse model (column 3) and the MRE for the fine model (last column). It is observed that the SM optimization converges to the solution after few fine model evaluations. The solutions for Crack1, Crack2, Pit1, and Pit2 are  $[15.13 \ 2.48]^T$ ,  $[35.11 \ 1.53]^T$ ,  $[3.09 \ 3.73]^T$ , and  $[5.01 \ 1.99]^T$ , which show MRE values of 0.8, 1.1, 6, and 1.2, respectively, when compared to the actual parameter values. These errors demonstrate significant improvement in the parameter estimation when compared with the MRE values obtained for coarse model optimal points.

Fig. 7 compares the target MFL responses with MFL responses obtained in optimal points for the coarse models, i.e.  $\mathbf{x}_c^*$ , and MFL responses obtained in SM optimal points, i.e.  $\bar{\mathbf{x}}_f$ , for all investigated defects.

In order to confirm the efficiency of the SM optimization in



getting fast and accurate results, we compare with direct optimization of the fine model. We choose  $[30 \ 3]^T$  and  $[4 \ 2.5]^T$  as the initial points for Crack1 and Pit1, respectively. The solutions via direct optimization of the fine model using SQP converges after 43 and 39 fine model evaluations for Crack1 and Pit1, respectively. The solutions found with the termination condition of (11) with  $\delta = 0.01$  are  $[25.9 \ 1.65]^T$  and  $[4.29 \ 2.66]^T$ , respectively. Corresponding values of MRE are 53 and 38, respectively. These large errors demonstrate that the direct optimization leads to the local minima in both cases, which are not the best solutions available. In contrast, SM optimization actually converges to the true solutions with the final result being of much smaller MRE. Also, these results indicate that the direct optimization of the fine model is far more computationally expensive than SM optimization.

It should be noted that a single FEM simulation takes about 1 hour of CPU time and 1.2 GB of memory using a 3.2 GHz Pentium 4 processor. This means that the direct optimization of the fine model requires in excess of 40 hours of CPU time. The direct optimization of the coarse model is very fast and takes just a few seconds, however, the resulting solutions are not acceptable in terms of the accuracy (typical MRE is about 30). Besides, 5 fine model evaluations (i.e., about 5 hours of the CPU time) are required to perform the coarse model scaling. On the other hand, space mapping optimization gives excellent results (typical MRE about 1) and requires only about 7 hours on average. This confirms that SM optimization is an efficient method of performing the inversion procedure in defect characterization.

## VI. CONCLUSION

In this work we present a space mapping optimization method to estimate defect parameters from MFL data. The proposed methodology was tested and verified for two common types of defects, rectangular cracks and cylindrical pits. The results demonstrated that there is a dramatic reduction in the number of fine model evaluations and therefore CPU time when using space mapping optimization instead of direct fine model optimization. Also, the results show that the proposed fast inversion technique features much improved accuracy, especially when compared to the results obtained using the analytical models.

Here, we have used simulated MFL signals as the target responses. In practice, a measured MFL response may be degraded by mechanical and electronic noise. This may lead to misalignment between fine model and actual measurements. Proper de-noising of the measured signal has to be employed prior to solving the inverse problem. Also, uncertainties in factors such as the B-H curve of the steel pipe, the lift-off distance of the magnetic sensor, the intensity of the excitation, etc., have to be considered. Such considerations would amount to an additional step in the inversion problem where the FEM simulations are aligned with the measured signal. From our experience [23] excellent alignment between FEM simulation and MFL measurements could be achieved with a simple multiplication of the whole data set by a single scaling (or calibration) factor. It takes into account the differences in the excitation sources employed in reality and in the simulations.

Furthermore, the described coarse models based on the analytical formulas are available only for specific types of defects. For arbitrary shape defects, other coarse models like a lightly-trained neural network or discretization of the defect shape to small canonical shapes with known coarse models could be used. This indicates that solving arbitrary shape defects is more involved and could be considered as our future research scope.

## REFERENCES

- [1] R. Schifini and A. C. Bruno, "Experimental verification of a finite element model used in a magnetic flux leakage inverse problem," *J. Phys.D: Appl. Phys.*, vol. 38, no. 12, pp. 1875-1880, June 2005.
- [2] Z. Chen, G. Preda, O. Mihalache, and K. Miya, "Reconstruction of crack shapes from the MFLT signals by using a rapid forward solver and an optimization approach," *IEEE Trans. Magn.*, vol. 38, no. 2, pp. 1025-1028, March 2002.
- [3] M. Yan, S. Udpa, S. Mandayam, Y. Sun, P. Sacks, and W. Lord, "Solution of inverse problems in electromagnetic NDE using finite element methods," *IEEE Trans. Magn.*, vol. 34, no. 5, pp. 2924-2927, September 1998.
- [4] C. Edwards and S. B. Palmer, "The magnetic leakage field of surface-breaking cracks," *J. Phys. D: Appl. Phys.*, vol. 19, no. 4, pp. 657-673, April 1986.
- [5] C. Mandache and L. Clapham, "A model for magnetic flux leakage signal Predictions," *J. Phys. D: Appl. Phys.*, vol. 36, no. 20, pp. 2427-2431, October 2003.
- [6] D. Minkov, J. Lee, and T. Shoji, "Study of crack inversions utilizing dipole model of a crack and Hall element measurements," *J. Magn. Mater.*, vol. 217, no. 1, pp. 207-215, July 2000.
- [7] D. Minkov, Y. Takeda, T. Shoji, and J. Lee, "Estimating the sizes of surface cracks based on Hall element measurements of the leakage magnetic field and a dipole model of a crack," *J. Appl. Phys. A*, vol. 74, no. 2, pp. 169-176, February 2002.
- [8] P. Ramuhalli, L. Udpa, and S. S. Udpa, "Electromagnetic NDE signal inversion by function-approximation neural networks," *IEEE Trans. Magn.*, vol. 38, no. 6, pp. 3633-3642, November 2002.
- [9] W. Han and P. Que, "2D defect reconstruction from MFL signals by a genetic optimization algorithm," *Russian J. of NDT*, vol. 41, no. 12, pp. 809-814, December 2005.
- [10] W. Han and P. Que, "Defect reconstruction of submarine oil pipeline from MFL signals using genetic simulated annealing algorithm," *J. Japan Petr. Inst.*, vol. 49, no. 3, pp. 145-150, 2006.
- [11] P. Ramuhalli, L. Udpa, and S. S. Udpa, "Neural network-based inversion algorithms in magnetic flux leakage nondestructive evaluation," *J. Appl. Phys.*, vol. 93, no. 10, pp. 8274-8276, May 2003.
- [12] A. Joshi, L. Udpa, S. S. Udpa, and A. Tamburrino, "Adaptive wavelets for characterizing magnetic flux leakage signals from pipeline inspection," *IEEE Trans. Magn.*, vol. 42, no. 10, pp. 3168-3170, October 2006.
- [13] J. W. Bandler, R. M. Biernacki, S. H. Chen, P. A. Grobelny, and R. H. Hemmers, "Space mapping technique for electromagnetic optimization," *IEEE Trans. Microw. Theory Tech.*, vol. 2, no. 12, pp. 2536-2544, December 1994.
- [14] J. W. Bandler, Q. S. Cheng, D. H. Gebre-Mariam, K. Madsen, F. Pedersen, and J. Søndergaard, "EM-based surrogate modeling and design exploiting implicit, frequency and output space mappings," in *IEEE MTT-S Int. Microw. Symp. Dig.*, Philadelphia, PA, June 2003, pp. 1003-1006.
- [15] J. W. Bandler, Q. S. Cheng, S. A. Dakrouy, A. S. Mohamed, M. H. Bakr, K. Madsen, and J. Søndergaard, "Space mapping: The state of the art," *IEEE Trans. Microw. Theory Tech.*, vol. 52, no. 1, pp. 337-361, January 2004.
- [16] D. Echeverria and P.W. Hemker, "Space mapping and defect correction," *CMAM The International Mathematical Journal Computational Methods in Applied Mathematics*, vol. 5, no. 2, pp. 107-136, 2005.

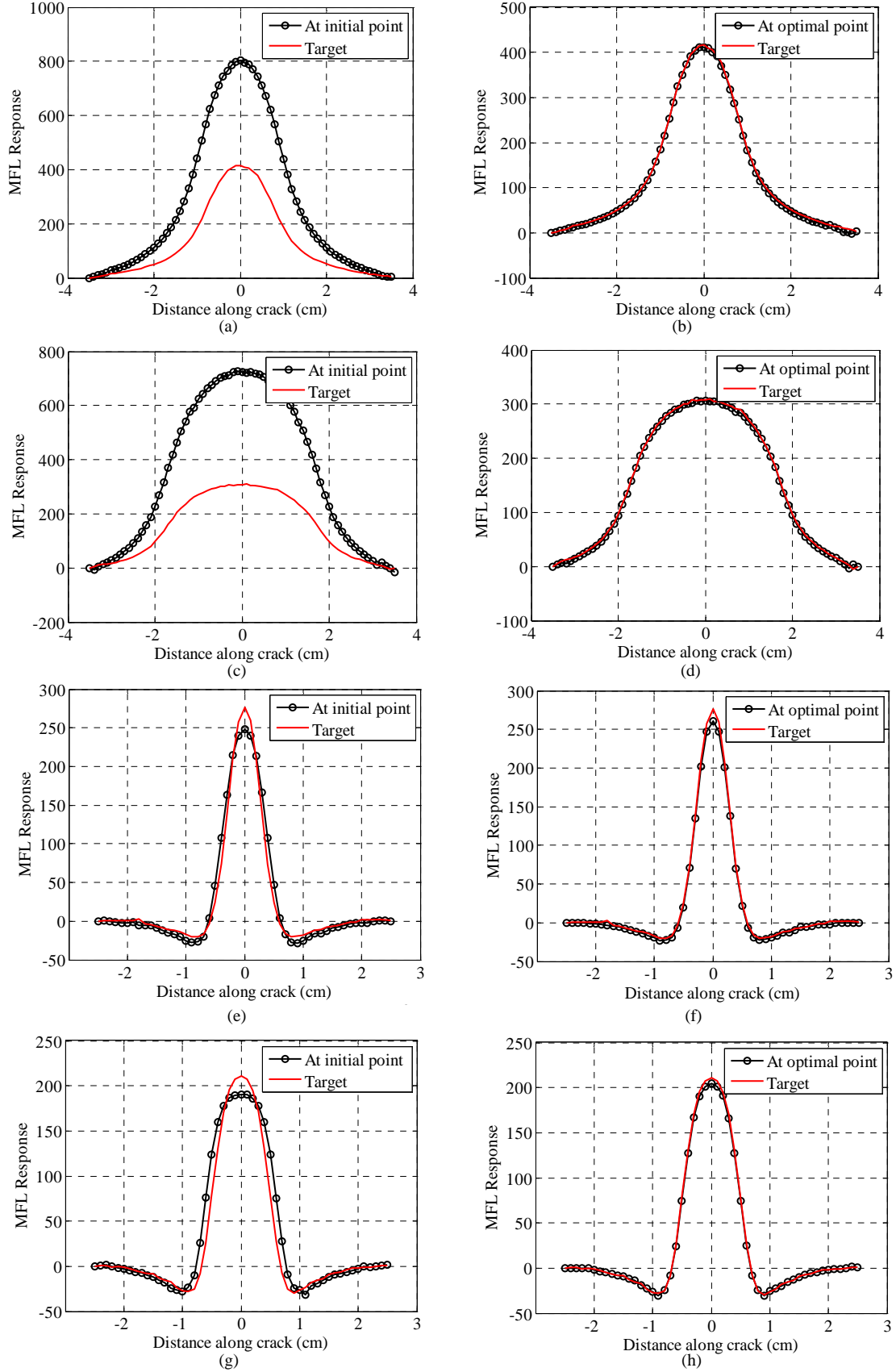


Fig. 7. Comparison of the target MFL response with MFL response obtained at the initial point  $x_c^*$ , i.e. coarse model optimal point, for: (a) Crack1, (c) Crack2, (e) Pit1, (g) Pit2; and comparison of the target MFL response with MFL response obtained at the SM optimal point  $\bar{x}_f$  for: (b) Crack1, (d) Crack2, (f) Pit1, (h) Pit2.



TABLE IV  
INVERSION RESULTS FOR SM OPTIMIZATION OF INVESTIGATED DEFECTS

Defect	Initial point ( $\mathbf{x}_c^*$ )	MRE for ( $\mathbf{x}_c^*$ )	No of SM Iterations	No of Fine Model Evaluations	Optimal point ( $\bar{\mathbf{x}}_f$ )	MRE for $\bar{\mathbf{x}}_f$
Crack1	$\begin{bmatrix} 17.38 \\ 3.53 \end{bmatrix}$	29	6	7	$\begin{bmatrix} 15.13 \\ 2.48 \end{bmatrix}$	0.8
Crack2	$\begin{bmatrix} 34.2 \\ 2.46 \end{bmatrix}$	33	6	7	$\begin{bmatrix} 35.11 \\ 1.53 \end{bmatrix}$	1.1
Pit1	$\begin{bmatrix} 4.13 \\ 2.62 \end{bmatrix}$	36	7	8	$\begin{bmatrix} 3.11 \\ 3.66 \end{bmatrix}$	6
Pit2	$\begin{bmatrix} 6.07 \\ 1.70 \end{bmatrix}$	18	3	4	$\begin{bmatrix} 5.00 \\ 1.95 \end{bmatrix}$	1.2

- [17] J. W. Bandler, S. Koziel and K. Madsen, "Space mapping for engineering optimization," *SIAG/Optimization Views-and-News Special Issue on Surrogate/Derivative-free Optimization*, vol. 17, no. 1, pp. 19-26, 2006.
- [18] S. Koziel, J. W. Bandler, and K. Madsen, "A space-mapping framework for engineering optimization: theory and implementation," *IEEE Trans. Microw. Theory Tech.*, vol. 54, no. 10, pp. 3721-3730, October 2006.
- [19] S. Amari, C. LeDrew, and W. Menzel, "Space-mapping optimization of planar coupled-resonator microwave filters," *IEEE Trans. Microwave Theory Tech.*, vol. 54, no. 5, pp. 2153-2159, May 2006.
- [20] G. Crevecoeur, L. Dupre, and R. Van de Walle, "Space mapping optimization of the magnetic circuit of electrical machines including local material degradation," *IEEE Trans. Magn.*, vol. 43, no 6, pp. 2609-2611, June 2007.
- [21] G. S. Park and E. S. Park, "Improvement of the sensor system in magnetic flux leakage-type nondestructive testing (NDT)," *IEEE Trans. Magn.*, vol. 38, no. 2, pp. 1277-1280, March 2002.
- [22] Maxwell Version 11.1.1, Ansoft Corporatin, <http://www.ansoft.com>, 2006.
- [23] R. K. Amineh, N. K. Nikolova, J. P. Reilly, and J. R. Hare, "Characterization of surface breaking cracks using one tangential component of magnetic leakage field," accepted for publication in *IEEE Trans. Magn.*
- [24] N. M. Alexandrov and R. M. Lewis, "An overview of first-order model management for engineering optimization," *Optimization Eng.*, vol. 2, no. 4, pp. 413-430, December 2001.
- [25] S. Koziel and J.W. Bandler, "Space-mapping optimization with adaptive surrogate model," *IEEE Trans. Microwave Theory Tech.*, vol. 55, no. 3, pp. 541-547, March 2007.
- [26] S. Koziel and J.W. Bandler, "Coarse and surrogate model assessment for engineering design optimization with space mapping," *IEEE MTT-S Int. Microwave Symp. Dig.*, Honolulu, HI, 2007, pp. 107-110.
- [27] Matlab<sup>TM</sup>, Version 7.1, The MathWorks, Inc., 3 Apple Hill Drive, Natick, MA 01760-2098, 2005.
- [28] S. Koziel and J.W. Bandler, "SMF: a user-friendly software engine for space-mapping-based engineering design optimization," *Int. Symp. Signals, Systems and Electronics, URSI ISSSE 2007*, pp. 157-160, 2007.
- [29] SMF, Bandler Corporation, P.O. Box 8083, Dundas, ON, Canada L9H 5E7, 2007.
- [30] R.H. Myers and D.C. Montgomery, "Response surface methodology: process and product optimization using designed experiments," John Wiley & Sons, Inc., New York, NY, 1995.